# Electrochemical performance of a symmetric supercapacitor device designed using laser-produced multilayer graphene

Gargi Dhiman[1], Kavita Kumari[2], Bon-Heun Koo[2], Faheem Ahmed[3], Nagih M. Shaalan[4,5], Saurabh Dalela[6], Parvez A. Alvi[7], Ranjeet Kumar Brajpuriya[1], Shalendra Kumar[1,*]

（1. *Department of Physics*, *School of Advanced Engineering*, *UPES*, *Dehradun* 248007, *India*;
2. *Industrial Technology Research Institute*, *Changwon National University*, *Changwon*, *Gyeongnam* 51140, *Republic of Korea*;
3. *Department of Applied Sciences and Humanities*, *Faculty of Engineering and Technology*, *Jamia Millia Islamia*, *New Delhi* 110025, *India*;
4. *Department of Physics*, *College of Science*, *King Faisal University*, *P.O. Box* 400, *Al-Ahsa* 31982, *Saudi Arabia*;
5. *Physics Department*, *Faculty of Science*, *Assiut University*, *Assiut* 71516, *Egypt*;
6. *Department of Pure & Applied Physics*, *University of Kota*, *Kota*, *Rajasthan* 324005, *India*;
7. *Department of Physical Science*, *Banasthali Vidyapith*, *Banasthali*, *Rajasthan*, 304022, *India*）

**Abstract**: We report an economical approach for the fabrication of laser-produced graphene (LPG) electrodes, which results in an improved electrochemical performance. Polyimide polymer was used as the starting material for LPG synthesis and was irradiated under ambient conditions with a $CO_2$ laser. The prepared LPG samples were characterized by Raman spectroscopy and FTIR, which validated the formation of multilayer graphene containing $sp^2$ hybridized C=C bonds. FE-SEM revealed three-dimensional (3D) sheet-like structures, while HR-TEM images showed lattice planes with an interplanar spacing of approximately 0.33 nm, corresponding to the (002) plane of graphene. Their electrochemical performance showed a remarkable areal specific capacitance ($C_A$) of 51 mF $cm^{-2}$ (170 F $g^{-1}$) at 1 mA $cm^{-2}$ (3.3 A $g^{-1}$) in a three-electrode configuration with 1 mol $L^{-1}$ KOH as the aqueous electrolyte. The LPG electrodes produced an energy density of ~3.5 μWh $cm^{-2}$ and a power density of ~350 μW $cm^{-2}$, demonstrating significant energy storage ability. They also had an excellent cycling stability, retaining 87% of their specific capacitance after 3 000 cycles at 1 mA/$cm^2$. A symmetric supercapacitor fabricated with LPG electrodes and the 1 mol $L^{-1}$ KOH electrolyte had a specific capacitance of 23 mF $cm^{-2}$ and showed excellent retention after 10 000 cycles, showing LPG's potential for use in supercapacitors.

**Key words:** Supercapacitors; Graphene; LPG; Electrochemical studies; Charge storage mechanism

## 1 Introduction

In recent times, the energy sector has faced unprecedented challenges due to ever-growing energy consumption and concerns over environmental sustainability. Consequently, the development of effective energy storage technologies has become crucial[1]. Electrochemical energy storage technology is of utmost importance in limiting the inherent inconsistencies of renewable energy sources and effectively meeting the escalating demands of contemporary society. Among the several energy storage technologies, supercapacitors (SCs) have gained a lot of attention because of their quick charging and discharging kinetics, substantial power density, extended lifespan, low input impedance, and environmental toughness. Researchers are continually engaged in enhancing the specific capacitance and energy density of SCs despite their many benefits. Generally, charge storage mechanisms in SCs take place by forming an electrostatic double layer (EDL) at the interface between an electrode and an electrolyte and/or pseudocapacitive process[2]. The electrode materials must exhibit favorable chemical kinetics, high chemical activity, reduced ion-diffusion path lengths, increased surface area, and numerous active sites for electrochemical reactions. For instance, Wang et al. synthesized 3D hierarchical *a*-$MnO_2$ nanotubes assembled hollow urchins, which provide electro-active sites and thereby find potential in improving the device performance[3]. However, the electrochemical performance of SCs is affected by structural deterioration and inadequate contact between the electrode-current collector con-

**Received date:** 2024-06-29; **Revised date:** 2024-09-20
**Corresponding author:** Shalendra Kumar. E-mail: shailuphy@gmail.com
**Author introduction:** Gargi Dhiman. E-mail: gargidhimaan@gmail.com

tact. Therefore, developing novel electrode components that can provide superior specific capacitance without any structural degradation is of utmost importance[4]. The emergence of carbon-based nanomaterials, specifically graphene, has drawn much attention as electrode material in SCs due to extensive surface area (hypothetical specific area of surface (SSA) of 2 675 $m^2/g$), higher porosity, superior electrical conduc divity, outstanding thermal stability and charge storage capability (hypothetical capacitance per unit mass of 550 F/g)[5-7]. Wang et al. demonstrated the synergistic effect of binder-free Prussian blue/ reduced graphene oxide (rGO) flexible electrodes which deliver a high specific capacitance of 286 F $g^{-1}$ and long-term cyclic durability[8]. Li et al. demonstrated a controlled synthesis of nitrogen and phosphorous co-doped carbon coated on rGO as an anode material which resulted in a high energy density of 107 Wh $kg^{-1}$ and ultra-durable cyclic stability[9]. Mi et al. demonstrated the synthesis of ultrafine amorphous Sb nanoparticles on rGO as anodes in sodium ion capacitors, which exhibited a $Na^+$ ion storage capacity of 83.5 mAh $g^{-1}$ showing high performance of Na-ion energy storage devices[10].

Numerous methodologies have been employed to fabricate graphene throughout the years, including the micromechanical exfoliation graphite, epitaxial growth on silicon carbide, Hummer's method, chemical vapor deposition, and its modified techniques for large-area graphene synthesis[11,12]. Nevertheless, many of the widely used techniques exhibit drawbacks, such as the need for intricate setups, the use of harsh chemicals, high temperatures, the dependence on costly and hazardous solvents, and finally, extended processing times[13]. Another challenge emerges in the electrode fabrication process, which usually requires, activated carbon and a binder, lowing the specific capacitance and consequently, impacts the SC device performance. To address these challenges associated with graphene synthesis and fabrication of electrodes, recently a new technique based on laser has been developed.

Recently, the utilization of laser technology to transform graphene oxide (GO) into graphene has gathered significant interest in areas of miniaturized as well as flexible systems of energy storage. This process involves the interaction of a laser beam with GO, resulting in the reduction of GO into graphene[14]. In 2014, Rice University researchers created Laser-Induced Graphene (LIG), a revolutionary synthesis method in which a $CO_2$ laser was exposed to Polyimide film. The intense heat generated by the laser converts the surface of polyimide into Graphene. This phenomenon involves the photothermal conversion of $sp^3$ carbon atoms of polyimide to $sp^2$ hybridized carbon atoms of graphene[15,16]. The resulting graphene synthesized using this method is useful for large-scale production, having a highly porous multi-layer 3D structure which makes it suitable for energy storage applications. Furthermore, enhanced electrochemical performance in SCs requires 3D porous structures which corresponds to the availability of highly conducting paths, providing high charge transfer rates[17,18]. Laser induced graphene (LIG) is widely sought-after as an electrode material thanks to its excellent mechanical strength, proficient electrical conductivity, enhanced surface area, as well as remarkable porosity[19]. For instance, micrometer-size graphene electrodes were developed on GO sheets through nano-writing by utilizing a femtosecond laser. This advancement opens up new possibilities for using graphene-derived materials in electrical microelectronics[20]. Similarly, scalable manufacturing of graphene-derived planar supercapacitors was revealed by EI-Kady et al., after utilizing a commercial LightScribe DVD burner which resulted in outstanding results[21]. In another study, Peng et al. synthesized B-doped graphene utilizing direct laser treatment, resulting in an increased areal capacitance[22]. Considering the exceptional performance of supercapacitors enhanced by laser-scribing technology for electrode synthesis and their direct utilization in SCs without adding any binder has opened new insights for future consumer electronics in SC applications.

This study involves the growth of laser-produced graphene (LPG) by employing a $CO_2$ laser for its use as electrodes in supercapacitor applications.

Structural investigation of LPG was performed using Raman spectroscopy, Fourier transform infrared spectroscopy (FTIR), field-emission scanning electron microscopy (FESEM), high-resolution transmission electron microscopy (HRTEM), and X-ray photoelectron spectroscopy (XPS). Using a three-electrode arrangement, the electrochemical performance of these electrodes is systematically evaluated. The electrochemical evaluation comprises crucial measurements using a three-electrode setup performed in 1 mol $L^{-1}$ KOH electrolyte. Charging/discharging cycles are assessed to evaluate the stability and durability of the electrode. Moreover, a symmetric supercapacitor device has been constructed to evaluate the efficacy of LPG as an electrode constituent in a cutting-edge supercapacitor application.

## 2 Experimental

### 2.1 Synthesis of laser-produced graphene (LPG)

The commercially flexible and non-conductive polyimide (PI) film, TapeCase, which has a thickness of 5.0 mil was used as the substrate as well as the carbon source. The $CO_2$ laser beam parameters are as follows: wavelength ($\lambda$) ~ 10.6 μm, maximum operating power of 40 W, and a scanning rate of 400 mm/s. Optimized laser power and head speed for synthesizing LPG are 9.0 W and 120 mm/s, respectively. Fig. 1 depicts a schematic representation of LPG on PI using a $CO_2$ laser. In this manner, multiple electrode pairs were inscribed onto a polymer sheet followed by cutting into single units (2 cm × 1 cm) and characterized subsequently. The whole process of fabrication was carried out under ambient conditions.

### 2.2 Material characterization

The Raman spectrum of LPG was carried out using a Raman Spectrophotometer (RIMS-U-DC) with an excitation of 532 nm. The laser spot size was nearly 1 μm, and the laser power was kept below 1 mW (to avoid local heating). FT-IR measurements of the LPG sample were conducted incorporating Perkin Elmer FTIR spectrometer which operates in the spectral region 400 to 4 000 $cm^{-1}$. An analysis of the morphology of the electrode was done by HR-FESEM (JSM-7900F, Jeol from Japan), operated at 15 kV potential. HRTEM from JOEL, model JEM-2100F, manufactured in Tokyo, Japan, was used to conduct the structural analysis. The operating voltage for the microscope was 200 kV. The LPG sample was mixed with ethanol and subjected to ultrasonicated for 15 min. Subsequently, 5 μL solution was carefully drop-casted on a copper grid coated with carbon and left to dry at ambient temperature for the TEM observation. Nitrogen adsorption/desorption isotherms at 77 K using an Anton Paar (Autosorb 6100 FKM MP-AG) equipment to perform Braunauer-Emmett-Teller (BET) surface area study. The material was degassed in a vacuum for 3 h at 200 °C, before BET analysis. The pore size distribution was assessed using the Barrett-Joyner-Halenda (BJH) method. XPS measurement was obtained on AXIS Supra + manufactured by Kratos Analytical Ltd. using a monochromatic Al $K_\alpha$ X-ray source.

### 2.3 Electrochemical measurements: Three-electrode configuration

Various electrochemical techniques, including cyclic voltammetry (CV), galvanometric discharge-charge (GCD), and electrochemical impedance spectroscopy (EIS) were employed to analyze the electrode's electrochemical behavior. The electrochemical response was evaluated with the help of the EC Biologic electrochemical workstation (EC-Lab V11.42). The experiments were initially conducted in

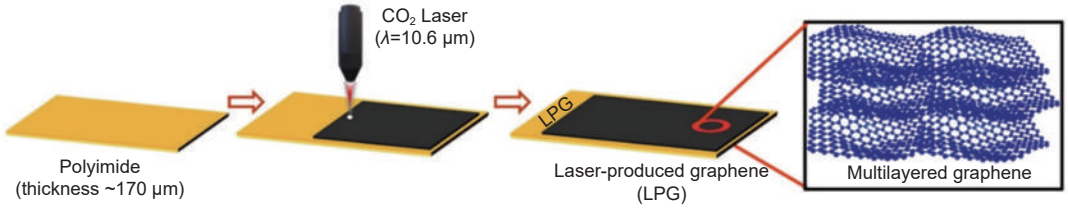


Fig. 1 Illustrative scheme of the LPG formation process

a 3-electrode arrangement using 1 mol $L^{-1}$ potassium hydroxide (KOH) electrolyte. In this setup, a platinum wire was used as the counter electrode, a saturated calomel electrode (Ag/AgCl) served as the reference electrode, and LPG was employed as the working electrode. CV experiments were conducted within the voltage range of 0 to 0.7 V at various scan rates ranging from 5 to 100 mV/s. The areal specific capacitance ($C_s$) (in mF/$cm^2$) based on CV measurements can be calculated by equation (1)[15].

$$C_s = \frac{1}{2 \times S \times v \times (V_f - V_i)} \int_{V_i}^{V_f} I(V)\,dV \quad (1)$$

where, $C_s$ = specific areal capacitance (mF $cm^{-2}$), $S$ denotes the electrode's active area (in $cm^2$), $V_f$ and $V_i$ signify the initial and final potential, $v$ represents voltage sweep per second (in V/s), and $I$(V) refers to the current (in milliamperes). $\int_{V_i}^{V_f} I(V)\mathrm{d}V$ equals polygon region calculated from CV curves.

The GCD measurements of LPG electrodes were carried out at 0 to 0.7 V voltage at different values of current per unit area (1 to 2.5 mA/$cm^2$). The specific areal capacitance ($C_s$), energy density ($E_s$) (μWh/$cm^2$), and power density ($P_s$) (μW/$cm^2$) according to the GCD test were evaluated by equations (2–4) respectively[23].

$$C_s = \frac{I}{S \times \mathrm{d}V/\mathrm{d}t} \quad (2)$$

$$E_s = \frac{1}{2} \times C_s \times \frac{(\Delta V)^2}{3600} \quad (3)$$

$$P_s = \frac{E_s}{\Delta t} \times 3600 \quad (4)$$

where, $C_s$ = specific capacitance in mF/$cm^2$; $I$ = discharge current in A/$cm^2$; $\frac{\mathrm{d}V}{\mathrm{d}t}$ denotes discharge time, and $S$ refers to the overall active area of electrodes.

The EIS tests were conducted within the frequency region of 0.1 Hz to 1 MHz in the three-electrode setup with a sinusoidal amplitude of 10 mV.

### 2.4 Fabrication of two-electrode device: Symmetric supercapacitor

The super-capacitive characteristics of the LPG electrode were evaluated by fabricating a symmetric SC device using a Swagelok cell assembly. The LPG powder was removed from the polyimide surface by scratching using a wired spatula and subsequently collected for electrode formation. Thereafter, a slurry was prepared containing LPG powder, PVDF (polyvinylidene difluoride) as a binder, and activated carbon in the ratio 8∶1∶1 by weight. All these components were combined using agate pestle and mortar and a small quantity of NMP (1-methyl-2-pyrrolidone) solvent to form a thick slurry. After that, the slurry was drop cast on a pair of circular-shaped graphitic paper with a diamter of 15 mm and was kept in an air oven at 80 °C to dry overnight. A Whatman filter paper as a separator of the same dimensions as that of electrodes was dipped in 1 mol $L^{-1}$ KOH electrolyte for 30 min. After that, the electrodes and the separator were assembled into the Swagelok cell, and a tiny dose of 1 mol $L^{-1}$ KOH aqueous electrolyte was introduced for the two-electrode device measurements as depicted in Fig. 7b. The CV and GCD were recorded in a voltage range of 0 to 0.8 V. The EIS test was conducted over a wide frequency range from 0.1 Hz to 1 MHz, with a 10 mV sinusoidal amplitude. The $C_s$, $E_s$, and $P_s$ were evaluated using the following equations[24].

$$C_s = \frac{2 \times I \times \Delta t}{S \times \Delta V} \quad (5)$$

$$E_s = \frac{C_s \times \Delta V^2}{2 \times 3.6} \quad (6)$$

$$P_s = \frac{E_s \times 3600}{\Delta t} \quad (7)$$

where $I$ represent the charging and discharging current, $\Delta t$ denotes the rate of discharge, $S$ represents the active area of the electrode material and $\Delta V$ signify voltage window.

## 3 Results and discussion

Raman spectra were taken to validate the nature of hybridization and to investigate the level of disorder, as well as the quantity of layers in LPG. The Raman spectrum of LPG within 1 000 to 3 000 $cm^{-1}$ range is depicted in Fig. 2a. The spectrum primarily contains $D$ and $G$ peaks and their overtones with no additional peaks are observed[25]. The $G$-peak centered at approximately 1 570 $cm^{-1}$, assigned to in-plane vibrations of $E_{2g}$ phonons of $sp^2$ hybridized C-atoms in the Brillouin zone center[26]. The $D$-peak is centered

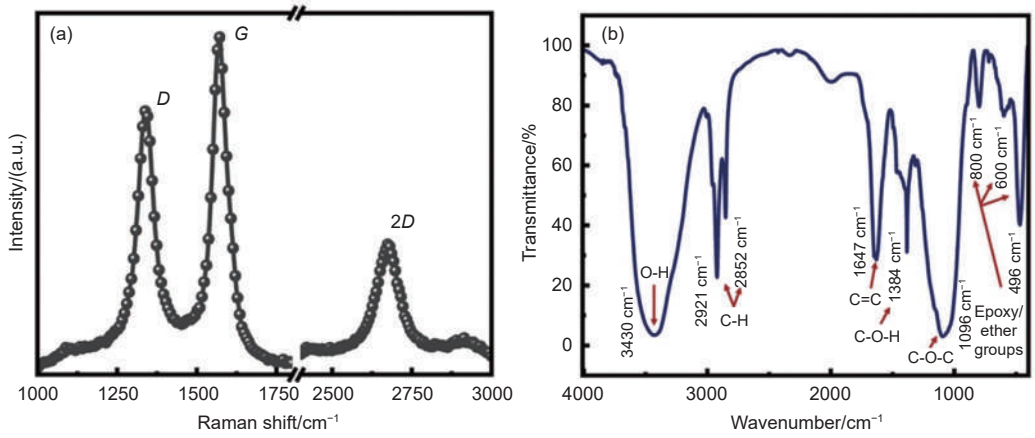


Fig. 2 (a) Raman spectrum of LPG. (b) FT-IR spectra of LPG.

around 1 348 $cm^{-1}$, associated with disordered graphitic structures due to the $sp^3$ bonds[27]. Furthermore, the 2nd order scattering of the *D*-band, named as the 2*D* band that appears at approximately 2 677 $cm^{-1}$, is utilized for the analysis of the stacking order in graphene[28]. Additionally, the number of layers and defect amount have been estimated using the intensity ratios $I_{2D}/I_G$ and $I_D/I_G$. The $I_{D/G}$ ratio ( ~ 0.8) confirms the presence of lattice defects in the LPG electrodes, possibly due to the vacancies, dislocations, and structural irregularities resulting from the high-energy laser pulses[29–31]. Moreover, the 3D porous structure of LPG contains dangling bonds, and other functional groups containing oxygen (such as epoxides, hydroxyls, or carbonyls) bonded to the graphene lattice, which provides additional active sites for charge storage as well as facilitating ion adsorption thereby improving the electrochemical properties of LPG[32]. The formation of multilayer graphene was confirmed by the $I_{2D/G}$ value, which is 0.5 (less than 1), permitting ion penetration into the stacked layers of graphene[33]. Additionally, the size of the crystallite ($L_a$) was computed using the following equation

$$L_a\,(\mathrm{nm}) = (2.4\times10^{-10})\lambda^4_{\mathrm{Laser}}\left(\frac{I_D}{I_G}\right)^{-1} \tag{8}$$

here, $\lambda$ represents the excitation wavelength of the laser. The aforementioned equation is obtained from the "Tuinstra Koenig Relation"[34]. The average $L_a$ was estimated as 24 nm, implying that laser-fabricated graphene has a significantly large crystallite size. This indicates high structural order and improved electrical conductivity, which facilitates faster charge transport and thus improves the overall electrochemical performance[35]. Similar findings were reported by Lin et al., revealing the presence of defects in graphene material synthesized via laser-induced method[15].

Fig. 2b displays the FTIR spectra of LPG, which were obtained to examine the presence of functional groups. The LPG powder was scratched and mixed with potassium bromide (KBr) in a 1 ∶ 100 ratio by mass and transformed into a transparent palette by applying suitable pressure. The observed absorption peak at 1 647 $cm^{-1}$ corresponds to C＝C bonds which are distinctive characteristics of graphene[36]. The additional vibrational peak at 3 430 $cm^{-1}$ suggests the appearance of a stretching mode associated with hydroxyl groups (O－H)[37]. The spectral peaks at 2 921 and 2 850 $cm^{-1}$ are indicative of the vibrational modes associated with the C－H bond in asymmetric ($aCH_2$) and symmetric ($sCH_2$) modes, respectively[38]. Additionally, the peaks observed at 1 384, 1 096 $cm^{-1}$, and in the range of 800–550 $cm^{-1}$ are attributed to the existence of C－O－H, C－O and other functional groups containing epoxy or ether at the boundaries of multilayer graphene[39]. Sindhu et al. reported similar results in LIG, identifying oxygen-containing functional groups that contribute to material's electrochemical properties[40].

Fig. 3a depicts the FESEM image of as-synthesized LPG. Notably, LPG possesseds the characteristic 3D multilayer structures. At higher magnification, as shown in the inset of Fig. 3a, the randomly oriented

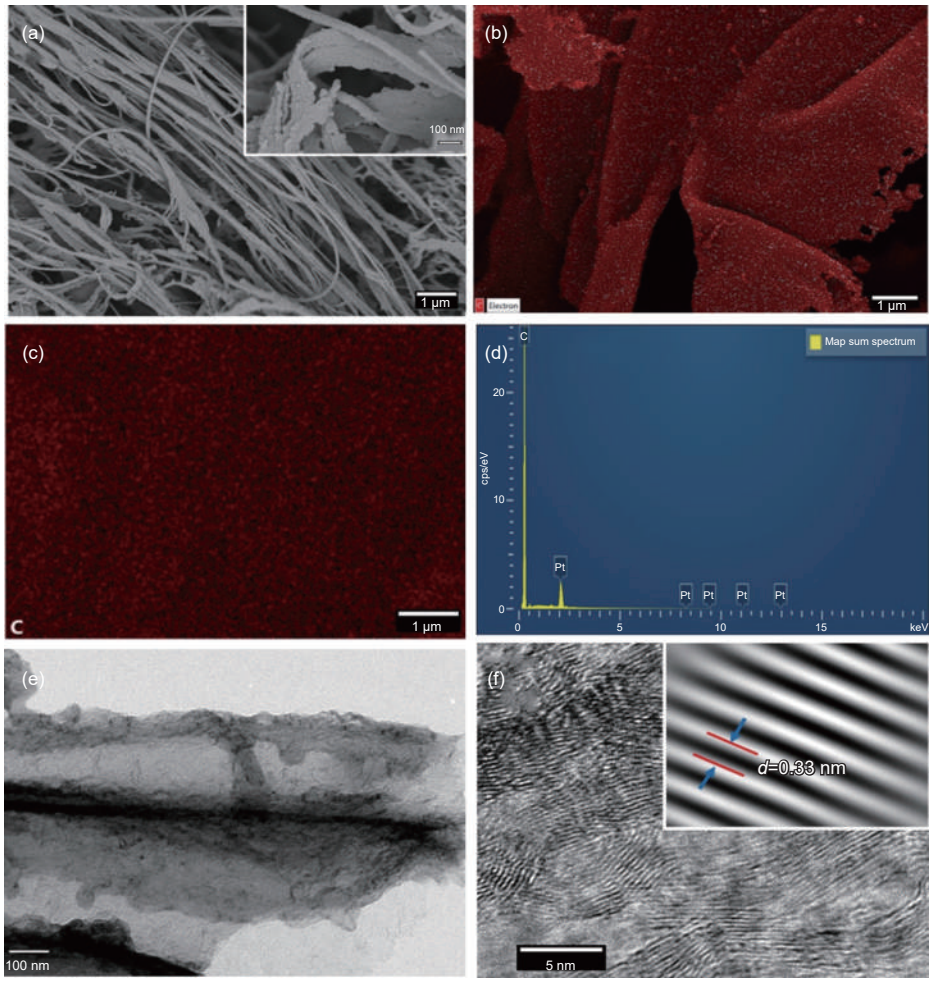


Fig. 3　(a) FESEM micrographs of as-prepared LPG and its magnified image in the inset. (b) EDS layered image of LPG. (c) Corresponding elemental mapping of LPG. (d) EDS spectrum of LPG. (e) TEM image of LPG. (f) HRTEM lattice fringes and the inset shows an enlarged image of atomic columns with an interplanar spacing of 0.33 nm

sheet-like structures of LPG are stacked together by weak Van der waals' forces. The particular morphology boosts the surface area of LPG, which enables the electrodes to accumulate more charges and also helps in forming an EDL. Furthermore, these 3D textures provided supplementary adsorption sites for KOH ions, resulting in enhanced electrochemical characteristics[41]. Fig. 3b, c represent the EDS layered image of LPG and the corresponding elemental mapping respectively, which illustrates the presence of carbon agreeing well with the Raman results. In addition, Fig. 3d displays the EDS spectrum of the LPG. The spectrum detected mainly carbon atoms. However, the appearance of Pt is due to the Pt coating on the surface of LPG for accurate detection of elements in EDS mapping. The interlinked graphene sheets demonstrate a porous morphology of LPG which increases ion transport phenomenon and charge storage properties.

Furthermore, the microstructural details of LPG were examined by TEM and HRTEM. Fig. 3e shows the TEM image of LPG, confirming the sheet-like multilayer structures of graphene formed by $CO_2$ laser. Additionally, the HRTEM micrograph depicted in Fig. 3f demonstrates the existence of elongated and curved ribbons or curved structures with width of 4–10 nm. The lattice fringes revealed the crystalline phase of LPG. Based on the enlarged section of the lattice planes as identified in the inset of Fig. 3f, the interlayer distance ($d$) is calculated to be 0.33 nm, which corresponds to (002) graphitic planar structure of LPG, as confirmed by the XRD study[42]. The equal alignment of the atomic plane implies the regular arrangement of carbon atoms in the atomic columns

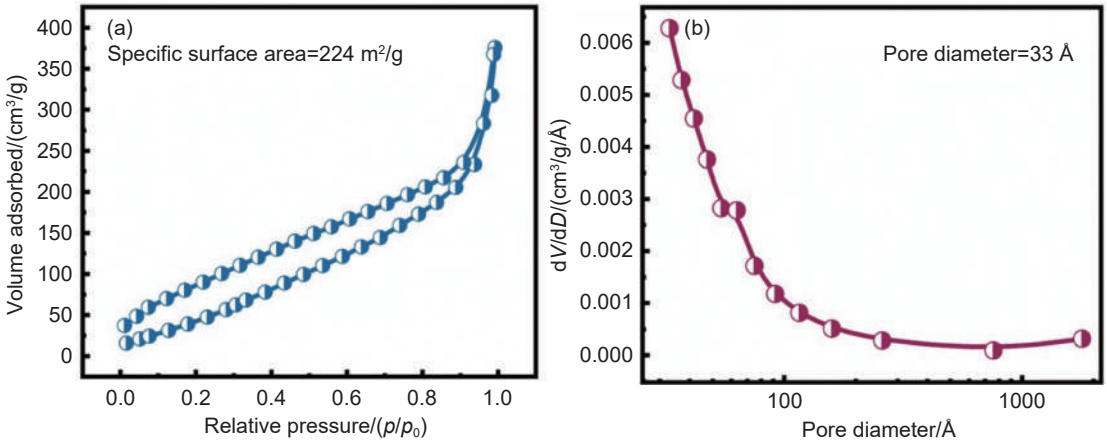


Fig. 4 (a) $N_2$ adsorption/desorption BET isotherm of LPG. (b) Pore size distribution of LPG

which lowers the resistance and promotes faster ion transport[43].

Nitrogen adsorption and desorption analysis were conducted on LPG to examine the specific surface area and pore size. Fig. 4a illustrates the characteristic type IV isotherm featuring a hysteresis loop of type H3, which signifies the porous characteristics of the material[44]. The BET-specific surface area for the LPG sample was calculated to be 224 $m^2/g$, exceeding previously reported values in the literature[45]. A broad BJH pore size distribution spanning from 3 to 180 nm suggests the existence of both mesoporous and microporous structures[46,47]. The pore volume of LPG was determined to be 0.565 $cm^3/g$, with a mean pore diameter of 33 Å, as illustrated by the pore distribution plot depicted in Fig. 4b. The porous morphology, along with a high surface area, promotes rapid ion transport and higher charge storage capacity, leading to superior electrochemical performance. Ryu et al. calculated the BET surface area for the densified LPG electrodes, which is estimated to be ~ 182 $cm^2/g$ and pore size ~ 4 nm[47]. Yuan et al. performed BET analysis for fluorine and boron-doped LPG and found a surface area ranging from approximately 164 to 210 $m^2/g$ and an average pore size of ~ 6.4 nm[48].

The XPS measurements are crucial to confirm the elemental composition and chemical state of the as-synthesized LPG samples. Fig. 5 displays the high-resolution XPS profile of C 1s spectra, with fitting performed using Shirley's background. The spectral peaks observed at 284.6, 285.3 and 288 eV can be attributed to the C=C, C−O and O−C=O bonds, respectively[49]. The predominant peak of 284.6 eV corresponds to the $sp^2$ hybridization of carbon atoms. The appearance of other peaks indicates the existence of oxygen-containing functional groups, such as hydroxyl and carbonyl, during the laser-induced process or due to the environmental exposure[50]. These findings provide evidence for the formation of 2D $sp^2$ geometry of carbon atoms which indicates graphene formation using the laser-based method along with oxygen-containing functional groups. These results are well-aligned with Raman spectroscopy and FTIR.

The electrochemical characteristics of the material were carried out using a 3-electrode arrangement in 1 mol $L^{-1}$ KOH electrolyte to assess their potential utilization as supercapacitors. Fig. 6a exhibits the CV curve of LPG with different sweep rates between 5 to 100 mV/s in the 0 to 0.7 V range. CV plot's response demonstrates capacitive characteristics, dis-

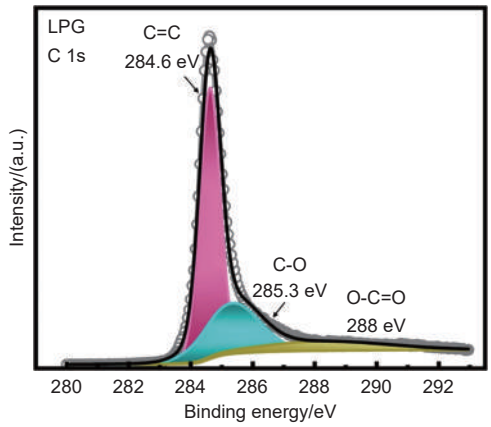


Fig. 5 XPS C 1s spectrum of LPG

playing quasi-rectangular loops instead of an ideal rectangular path. No redox peaks appeared in the tested potential window, which indicates excellent capacitive properties. The region covered by CV curves was employed to calculate the specific capacitances. Fig. 6b depicts the variance of specific capacitance and the voltage sweep rate. Moreover, the specific capacitance exhibits an inverse relation with sweep voltage. This behaviour occurs due to the reduced efficacy of ion penetration into the LPG electrodes at elevated sweep rates. Whereas, when the voltage scan rate is reduced, ions from the electrolyte effectively and quickly enter the gaps between the layers of multilayer graphene, resulting in high specific capacitance[51]. Also, as the sweep rate rises, the ohmic resistance of aqueous electrolyte ions in the pores increases, resulting in a decrease in the calculated value of capacitance[52]. Moreover, the presence of defects in LPG may affect its electrochemical performance. High porosity, along with substantial surface area of LPG electrodes, contributes to its capacitive properties.

The electrochemical characteristics of the LPG electrodes were further confirmed by GCD analysis. Fig. 6c represents the GCD graph that exhibited a quasi-triangular symmetrical distribution, suggesting the strong reversibility of the electrode material, which is also a typical feature of capacitive behavior in supercapacitors[53]. The GCD test of LPG was conducted at various values of specific current in the range 1 to 2.5 mA/cm$^2$, within a similar potential range as that of CV measurements. At 1 mA/cm$^2$, the areal capacitance was calculated as ~ 51 mF/cm$^2$ (171 F/g). Furthermore, when increasing the value of the specific current to 1.25 mA/cm$^2$, the areal specific capacitance is calculated to be ~ 24 mF/cm$^2$. These findings are well aligned with the CV results. Additionally, the decrease in specific capacitance are seen with an increment in specific current (Fig. 6d). Similar findings were reported by Shaalan et al. while testing the electrochemical performance of NiO-doped LPG electrodes[42]. This behaviour may be ascribed to the limited timeframe for the ions to permeate the in-

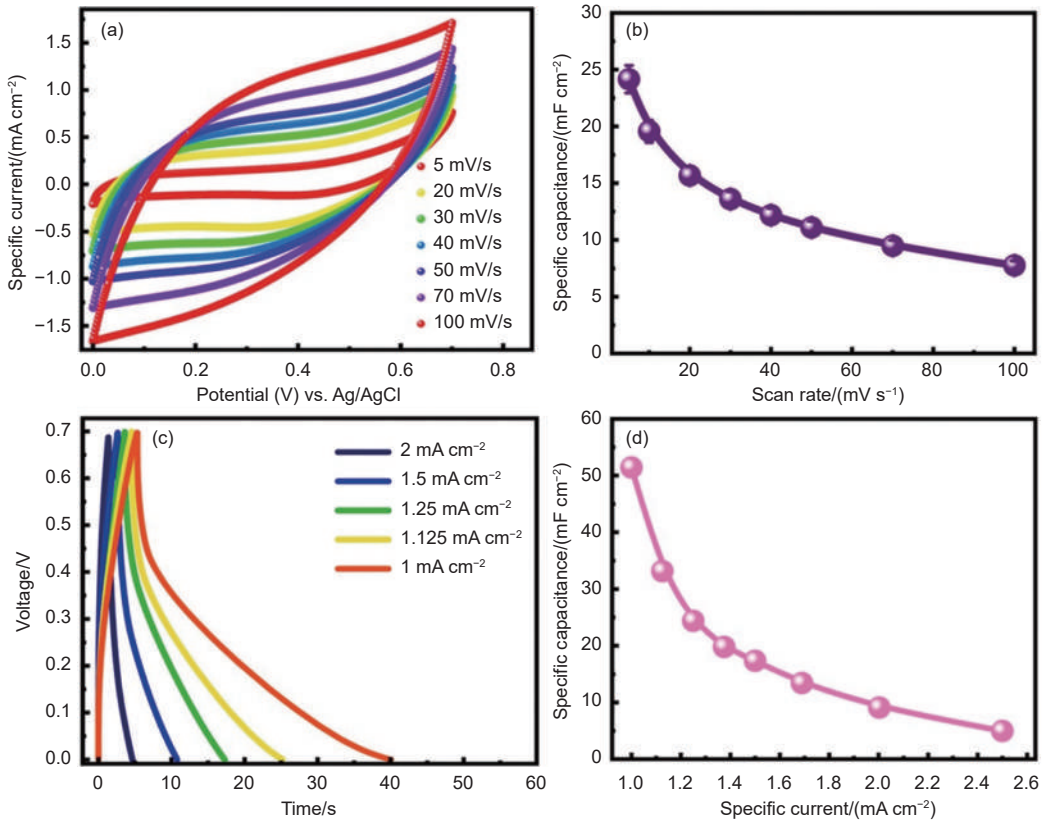


Fig. 6　(a) CV curves of LPG at various scan rates from 5 to 100 mV s$^{-1}$. (b) Variation of specific capacitance at different scan rates. (c) GCD curves for LPG electrode at various current densities, and (d) variation of specific capacitance at different values of specific current

ternal sheet-like structures of the multilayer LPG electrode at a higher value of current. The asymmetry observed in charge-discharge curves can be attributed to the presence of oxygen-containing functional groups, such as carbonyl (C＝O), carboxyl (－COOH) and hydroxyl (－OH). These groups participate in reversible redox reactions, leading to an extended discharge time. These side reactions are responsible for coulombic efficiency exceeding 100%[54,55].

To further investigate the ion storage mechanism, the respective contributions of surface-controlled and diffusion-controlled processes are estimated. The methodology developed by Trasatti et al. evaluates the charge storage processes by examining the voltammetric charge, which is produced through 2 sources[56]. The surface-controlled process (EDLC) occurs at the interface, whereas, the other process signifies the insertion/extrusion of ions in the bulk electrode materials. Fig. 7a illustrates the percentage contribution of specific capacitance. It represents a CV plot at 50 mV/s and reflects the contributions from both processes. Based on the analysis, it is evident that the diffusion-controlled process is dominating in LPG, accounting for 93% of the overall contribution, while the surface-controlled process only contributes 7% (Fig. 7b). Fig. 7c displays a schematic diagram depicting the three-electrode setup and a detailed mechanism to gain insight into the migration of $K^+$ and $OH^-$ ions into the multilayer graphene. The sheet-like structure of 3D multilayer graphene enables the penetration of $K^+$ and $OH^-$ ions into the randomly coiled layered structures of LPG. However, recently, certain research groups have made initiatives to control the distribution of pore diameters in nanomaterials, to enhance the effective diffusivity and increase active sites for the effective insertion of electrolytes into the layers of nanostructures[57,58].

Another crucial indicator for assessing the quality of the electrode is its cyclic performance. Fig. 8a demonstrates the areal capacitance in accordance with the cycle number of the LPG at 1 mA/cm$^2$. Following 3 000 cycles, the areal-specific capacitance LPG electrode shows slight attenuation from 51 mF/cm$^2$ to 44.3 mF/cm$^2$, and the corresponding retention rate is

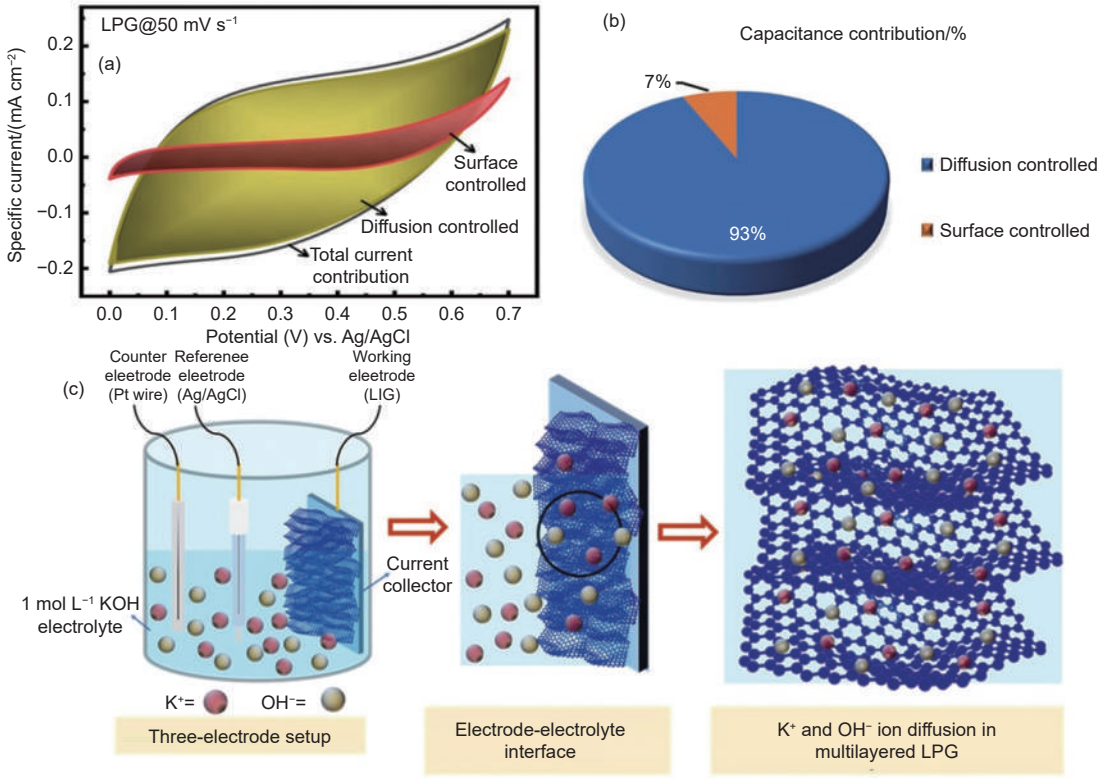


Fig. 7 (a) Trasatti method analysis of capacitance contribution. (b) 3D pie chart showing percentage contribution of capacitance. (c) Schematic illustration of three-electrode setup, and charge storage mechanism in LPG

found to be 87% after 3 200 cycles as presented in Fig. 8b. During the initial cycles, the areal capacitance increases, due to the increased accessibility of electrolyte ions within the electrode. As the number of cycles evolves, the areal capacitance of the electrode material decreases due to the deterioration of the material and an increased internal resistance, which erodes its electrochemical performance. Fig. 8c displays the Ragone plot illustrating the relation between specific energy and specific power. The LPG electrodes deliver a maximum of 3.5 μWh/cm$^2$ specific energy at a specific power of 350 μWh/cm$^2$, which is better than the results reported in the previous study. A comparative analysis of LPG with other materials is given in Table 1.

The Nyquist plot obtained from EIS is shown in Fig. 8d. The simulation was performed using *Z* view 4.0 software and the corresponding equivalent circuit for the system containing electronic components. *Z*' symbolizes the real impedance, while *Z*'' stands for the

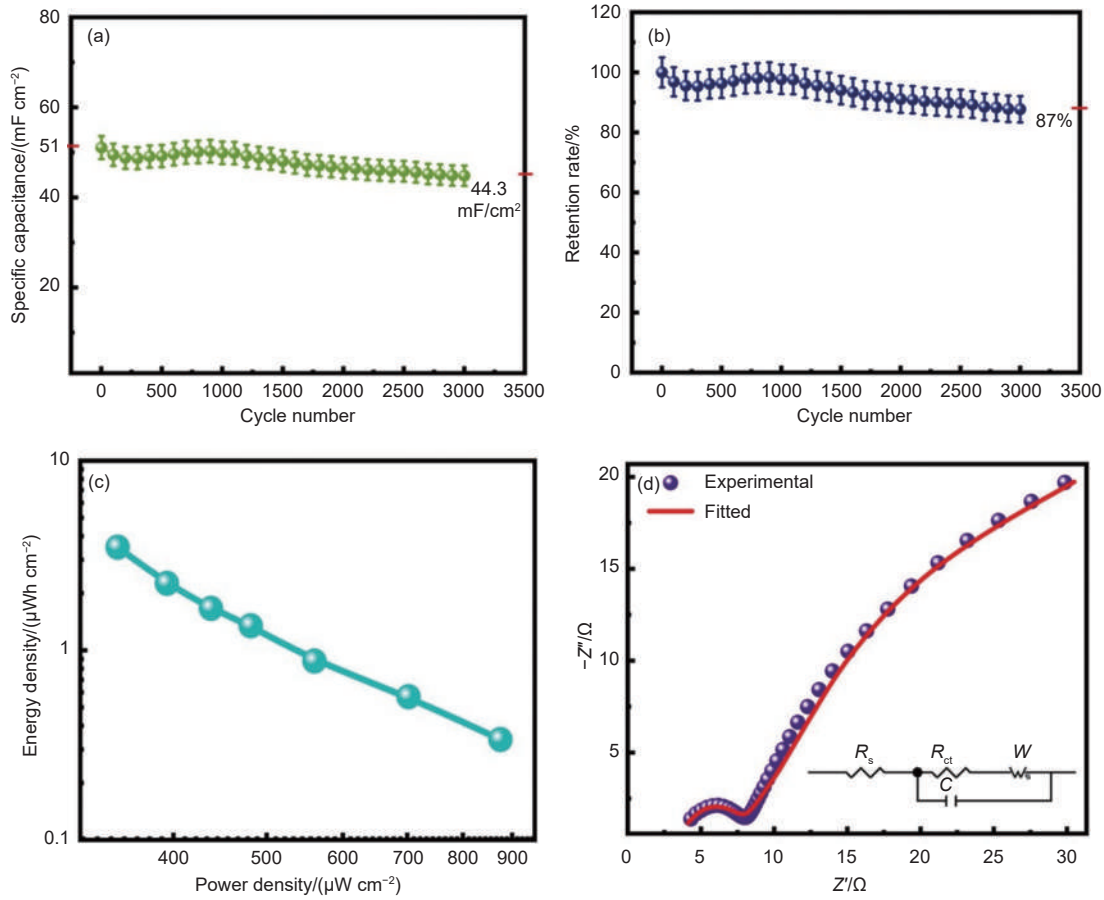


Fig. 8　(a) Cyclic performance of LPG in three-electrode-configuration after 3 000 cycles at 1 mA cm$^{-2}$. (b) Retention rate vs cycle number. (c) Ragone plot of LPG at 1 mA cm$^{-2}$. (d) Nyquist plot of LPG in the frequency range 0.1 Hz to 1 MHz

**Table 1　Comparative analysis of electrochemical performance of different materials using three-electrode measurements**

| Material | Synthesis method | Specific capacitance/ (mF cm$^{-2}$) | Energy density/ (μWh cm$^{-2}$) | Retention rate/(%) | Reference |
|---|---|---|---|---|---|
| **Laser-Produced Graphene (LPG)** | **$CO_2$ laser on PI** | **51** | **3.5** | **93** | **This work** |
| Graphene oxide (GO) | Hummer's method | 35 | 1.3 | 85 | [59] |
| Reduced graphene oxide (rGO) | Modified hummer's method | 80 | 2.5 | 87 | [60] |
| Activated carbon (AC) | Activation of carbon precursors | 40 | 2.0 | 85 | [61] |
| $MnO_2$/graphene composite | Hydrothermal method | 120 | 4.0 | 95 | [62] |
| Conductive polymer (Polyaniline) | Chemical polymerization of aniline | 50 | 2.5 | 80 | [63] |
| Transition metal oxide ($RuO_2$) | Sol-gel synthesis | 200 | 5.0 | 90 | [64] |
| Heteroatom-doped graphene | Chemical vapor deposition (CVD) | 90 | 3.5 | 92 | [65] |

imaginary impedance. In addition, $Z'$ represents the resistance of the electrolyte ($R_s$), the resistance of charge transfer ($R_{ct}$), and the Warburg resistance ($W_{o\text{-}R}$). Within the realm of intermediate and higher frequencies, the arc diameter signifies the transfer of charge ($R_{ct}$). On the other hand, in the higher-frequency regime, the x-intercept reveals the overall resistance ($R_s$), encompassing the resistance offered by the electrode materials, the electrolyte's ionic resistance, and the resistance at the contact point between the electrode and the current collector. The total internal resistance ($R_s$) and charge transfer resistance are found to be 3.5 and 3.7 Ω respectively. In the middle-frequency range, there is a diagonal curve which signifies the Warburg impedance ($W$). This curve indicates the ion movement in the electrolyte, either through diffusion or transportation. In the low-frequency region, the electrode demonstrates capacitive behaviour[35].

To determine the practical application of the LPG electrode, a symmetric SC was designed using a Swagelok cell assembly in 1 mol $L^{-1}$ KOH aqueous electrolyte. Fig. 9a reveals the CV profile of the electrode acquired at various scan rates varying from 5 to 100 mV/s. The symmetrical and quasi-rectangular pattern indicate capacitive characteristics analogous to the findings observed in the 3-electrode test. Fig. 9b conveys the correlation between scan rate and specific capacitance, indicating a substantial decline in specific capacitance as scan rates increase. Fig. 9c, d display the LPG device's charging-discharging profile at different specific currents. The obtained maximum specific capacitance of 23 mF/cm$^2$ (41 F/g) at 0.15 mA/cm$^2$ demonstrates significant improvement compared to the recently reported values in the scientific literature (Table 2). Fig. 10a shows the specific capacitance concerning the cycle number of the LPG electrode material at 0.15 mA/cm$^2$. After 10 000 cycles, the areal-specific capacitance and capacitance retention are depicted in Fig. 10b, which suggests that

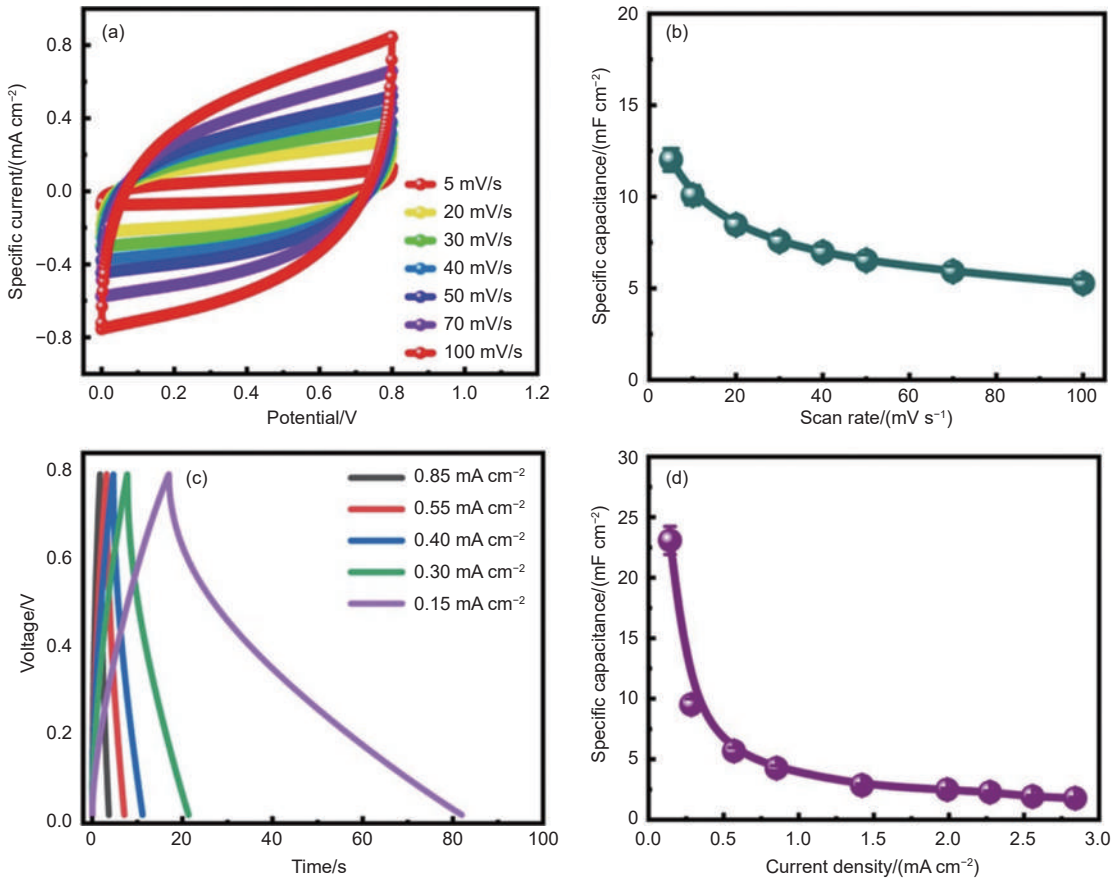


Fig. 9 (a) CV curve of LPG device at various scan rates from 5 to 100 mV $s^{-1}$. (b) Variation of specific capacitance at different scan rates. (c) GCD curves for LPG electrode in device at various current densities, and (d) variation of specific capacitance at different values of specific current

LPG electrodes deliver 95% capacitance retention. The initial spike in specific capacitance is due to the diffusion-controlled contribution, while a gradual decline takes place in subsequent cycles. The highly porous structure, significant surface area, and superior electrical conductivity of graphene contribute to the remarkable cyclic stability of the electrodes[66]. Fig. 10c displays the Ragone plot that shows the variation of specific energy with specific power exhibiting a linear variation. The LPG electrodes deliver a maximum energy density of 2 μWh/cm$^2$ at 113 μW/cm$^2$ power density and a maximum power density of 2 273 μW/cm$^2$ at 0.15 μWh/cm$^2$ energy density. The $C_s$, $E_s$ and retention rate of three-electrode and device measurements are summarized in Table 3.

The EIS investigations were displayed in the form of a Nyquist plot (Fig. 10d), before and after cycles 3 000 cycles to examine the $R_s$ and $R_{ct}$ resistances of the device. The EIS curves exhibit a consistent pattern, involving a very small semi-circle, representing $R_{ct}$, and a straight line, indicating $W$ due to a diffusion-controlled process at the interface. The analogous circuit was simulated utilizing Zview software.

**Table 2　Electrochemical performance of Graphene-based supercapacitors in two-electrode device**

| Electrode material (Graphene-based) | Electrolyte | Specific capacitance of device | Reference |
|---|---|---|---|
| LIG microsupercapacitor | PVA gel electrolyte | 22.2 mF cm$^{-2}$ at 0.05 mA cm$^{-2}$ | [62] |
| Graphene on PI | Aqueous electrolyte (KOH) | 2.19 mF cm$^{-2}$ at 0.263 mA cm$^{-2}$ | [67] |
| LIG on PI | Gel electrolyte | 800 μF cm$^{-2}$ at 10 mV/s | [68] |
| LIG + MWCNT | Gel electrolyte | 11.17 mF cm$^{-2}$ at 0.2 mA cm$^{-2}$ | [69] |
| LIG + PG | Gel electrolyte | 3.39 mF cm$^{-2}$ at 15.6 μA cm$^{-2}$ | [1] |
| Densified LIG | $H_2SO_4$ gel electrolyte | 19.5 mF cm$^{-2}$ at 0.05 mA cm$^{-2}$ | [47] |
| **LPG** | **1 mol L$^{-1}$ KOH aqueous electrolyte** | **23 mF cm$^{-2}$ at 0.15 mA cm$^{-2}$** | **This work** |

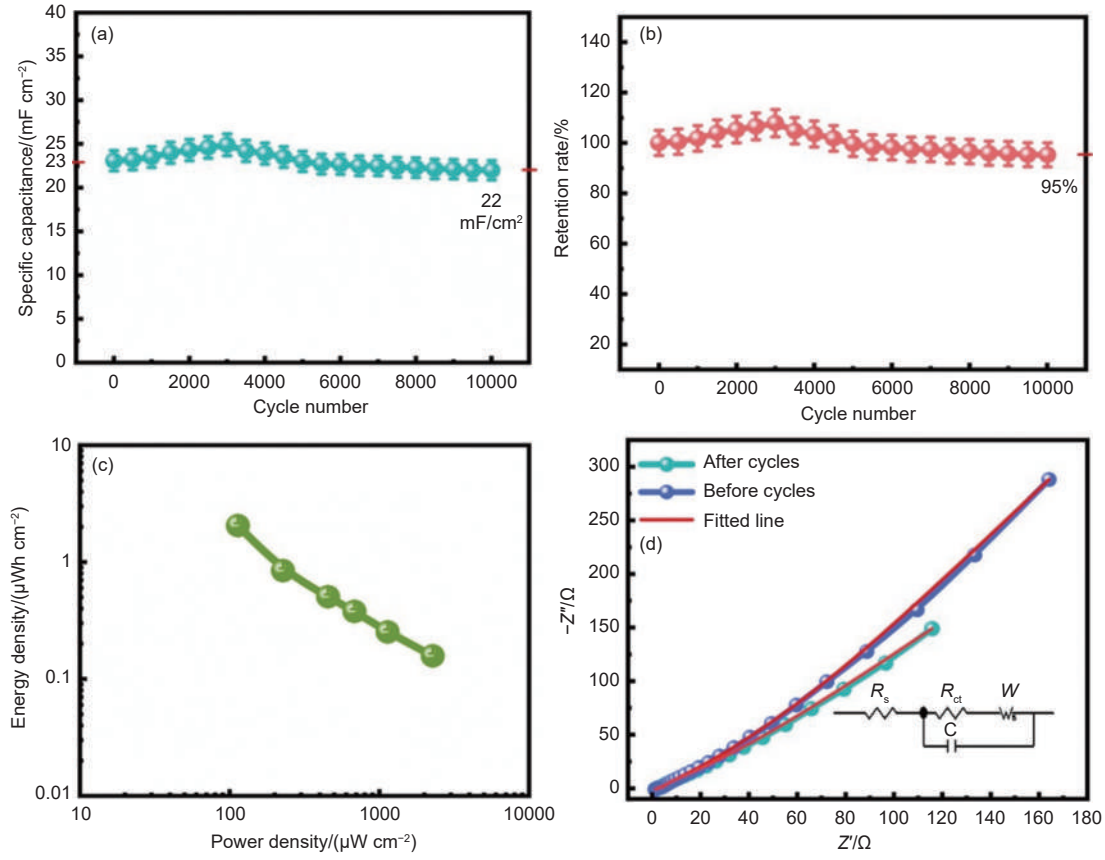


Fig. 10　(a) Cyclic performance of LPG device after 10 000 cycles at 0.15 mA cm$^{-2}$. (b) Retention rate vs cycle number. (c) Ragone plot of LPG utilized in device. (d) Nyquist Plot of LPG in the frequency range 0.1 Hz to 1 MHz before and after 10 000 cycles with circuit fitting using Zview software

**Table 3 Summary of maximum values of areal specific capacitance ($C_s$), energy density ($E_s$), and retention rate of LPG electrode in three-electrode configuration and device**

| Measurements | Three-electrode setup | Device |
|---|---|---|
| Specific capacitance ($C_s$) | 51 mF $cm^{-2}$ | 23 mF $cm^{-2}$ |
| Energy density ($E_s$) (at power density) | 3.5 μWh $cm^{-2}$ at (350 μWcm$^{-2}$) | 2 μWh $cm^{-2}$ at (113 μWcm$^{-2}$) |
| Retention rate (%) | 87% (3 000 cycles) | 95% (10 000 cycles) |

The EIS results for the LPG device as a symmetric SC device are well-aligned with the findings obtained from 3-electrode analysis. Fig. 10d reveals that $R_s$ is 2 Ω before and after cycles, whereas the $R_{ct}$ decreases from 1.5 to 0.5 Ω after 3 000 cycles. The slight deviation of the linear trajectory in the low-frequency range following 3 000 cycles primarily arises from the repulsive resistive impact caused by the presence of occupied ions in the 3D sheet-like structures of the LPG electrode.

## 4 Conclusion

Herein, a facile and economical approach was developed for the synthesis of LPG. The fabricated sample was examined using Raman spectroscopy, FT-IR, FESEM, HRTEM and XPS. This confirms the formation of multilayer graphene with few defects and a highly porous nature. Moreover, the 3D sheet-like structures in the multilayer LPG demonstrated impressive capacitive properties. Using a three-electrode configuration, the electrode exhibited a maximum areal-specific capacitance of 51 mF $cm^{-2}$ (170 F $g^{-1}$) at 1 mA $cm^{-2}$ in a 1 mol $L^{-1}$ KOH electrolyte. Furthermore, the LPG electrode material produces an excellent energy density of 3.5 μWh $cm^{-2}$ at a power density of 350 μW $cm^{-2}$. The cyclic stability of the electrodes was measured to be 93% after 1 000 cycles at 1 mA $cm^{-2}$, demonstrating highly stable device performance. Furthermore, the LPG-symmetric SC showed excellent performance with 23 mF $cm^{-2}$ areal capacitance at 0.15 mA $cm^{-2}$. However, there is potential for further enhancement of these SC electrodes by developing composite materials or doping with other pseudocapacitive/battery-like materials and selecting suitable electrolytes. This study not only presents a high-performance SC, but also provides charge storage mechanism in LPG electrodes, unlocking its potential as a cutting-edge electrode material in SC applications.

## Declarations

The authors affirm that they possess no conflicting interests.

## Acknowledgements

One of the authors, Gargi Dhiman, would like to acknowledge UPES, Dehradun, for providing PhD fellowship and SEED Grant.

**References**

[1] Anagbonu P, Ghali M, Allam A. Low-temperature green synthesis of few-layered graphene sheets from pomegranate peels for supercapacitor applications[J]. Scientific Reports, 2023, 13: 15627.

[2] Lokhande P E, Chavan U S, Pandey A. Materials and fabrication methods for electrochemical supercapacitors: Overview[J]. Electrochemical Energy Reviews, 2019, 3(1): 155-186.

[3] Wang J G, Yang Y, Huang Z H, et al. Shape-controlled synthesis of hierarchical hollow urchin-shape α-$MnO_2$ nanostructures and their electrochemical properties[J]. Materials Chemistry and Physics, 2013, 140: 643-650.

[4] Shifei H, Zhu X, Sarkar S, Zhao Y. Challenges and opportunities for supercapacitors[J]. APL Materials, 2019, 7: 100901.

[5] Novoselov K S, Geim A K, Morozov S V, et al. Electric field in atomically thin carbon films[J]. Science, 2004, 306: 666-669.

[6] Narayanan R, Yamada H, Karakaya M, et al. Modulation of the electrostatic and quantum capacitances of few layered graphenes through plasma processing[J]. Nano Letters, 2015, 15: 3067-3072.

[7] Dou H L, Zhao Z X, Yang S B, et al. The role of carbon materials in suppressing dendrite formation in lithium metal batteries[J]. New Carbon Materials, 2023, 38: 599-618.

[8] Wang J G, Ren L, Hou Z, et al. Flexible reduced graphene oxide/Prussian blue films for hybrid supercapacitors[J]. Chemical Engineering Journal, 2020, 397: 125521.

[9] Li T, Huang X, Lei S, et al. Two-dimensional nitrogen and phosphorus co-doped mesoporous carbon-graphene nanosheets anode for high-performance potassium-ion capacitor[J]. Energy Materials, 2023, 3(2): 300018.

[10] Mi C, Qin Y, Huang X, et al. Galvanic replacement synthesis of graphene coupled amorphous antimony nanoparticles for high-

performance sodium-ion capacitor[J]. Acta Physico - Chimica Sinica, 2024, 40(5): 2306011.

[11] Mbayachi V B, Ndayiragije E, Sammani T, et al. Graphene synthesis, characterization, and its applications: A review[J]. Results in Chemistry, 2021, 3(10): 100163.

[12] Faggio G, Messina G, Lofaro C, et al. Recent advancements on the CVD of Graphene on copper from ethanol vapor[J]. C — Journal of Carbon Research, 2020, 6(1): 14.

[13] Velasco A, Ryu Y K, Hamada A, et al. Laser-induced graphene microsupercapacitors: structure, quality, and performance[J]. Nanomaterials, 2023, 13(5): 788.

[14] Zhang Y L, Guo L, Xia H, et al. Photoreduction of graphene oxides: methods, properties, and applications[J]. Advanced Optical Materials, 2014, 2: 10-28.

[15] Lin J, Peng Z, Liu Y, et al. Laser-induced porous graphene films from commercial polymers[J]. Nature Communications, 2014, 5: 5714.

[16] Ye R, James D K, Tour J M. Laser-Induced Graphene: From Discovery to Translation[J]. Advanced Materials, 2019, 31(1): 1803621.

[17] Wu Z S, Sun Y, Tan Y Z, et al. Three-dimensional graphene-based macro- and mesoporous frameworks for high-performance electrochemical capacitive energy storage[J]. Journal of American Chemical Society, 2012, 134(48): 19532-19535.

[18] Wu M, Meng S, Wang Q, et al. Nickel-cobalt oxide decorated three-dimensional graphene as an enzyme mimic for glucose and calcium detection[J]. ACS Applied Materials and Interfaces, 2015, 7(38): 21089-21094.

[19] Wang Y, Luo J L, Lu Z H, et al. A review of the high-concentration processing, densification, and applications of graphene oxide and graphene[J]. New Carbon Materials, 2024, 39(3): 483-505.

[20] Liu Z B, Li L, Xu Y F, et al. Direct patterning on reduced graphene oxide nanosheets using femtosecond laser pulses[J]. Journal of Optics, 2011, 13(8): 085601.

[21] El-Kady M F, Kaner R B. Scalable fabrication of high-power graphene micro-supercapacitors for flexible and on-chip energy storage[J]. Nature Communications, 2013, 4: 1475.

[22] Peng Z, Ye R, Mann J A, et al. Flexible boron-doped laser-induced graphene micro supercapacitors[J]. ACS Nano, 2015, 9(6): 5868-5875.

[23] Lin J, Zhang C, Yan Z, et al. 3-dimensional graphene carbon nanotube carpet-based micro-supercapacitors with high electrochemical performance[J]. Nano Letters, 2013, 13(1): 72-78.

[24] Bulla M, Kumar V, Devi R, et al. Natural resource-derived NiO nanoparticles via aloe vera for high-performance symmetric supercapacitor[J]. Scientific Reports, 2024, 14: 7389.

[25] Ferrari A C, Basko D M. Raman spectroscopy as a versatile tool for studying the properties of graphene[J]. Nature Nanotechnology, 2013, 8: 235-246.

[26] Dell'anna R, Iacob E, Tripathi M, et al. AFM and Raman study of graphene deposited on silicon surfaces nanostructured by ion beam irradiation[J]. Journal of Microscopy, 2020, 280(3): 183-193.

[27] Ferrari A C, Robertson J. Raman spectroscopy of amorphous, nanostructured, diamondlike carbon, and nanodiamond[J]. Philosophical Transactions of the Royal Society of London Series A: Mathematical, Physical and Engineering Sciences, 2004, 362(1824): 2477-2512.

[28] Pattanayak B, Le P A, Panda D, et al. Ion accumulation-induced capacitance elevation in a microporous graphene-based supercapacitor[J]. RSC Advances, 2022, 12: 27082-27093.

[29] Shaalan N M, Ahmed F, Kumar S, et al. Monitoring food spoilage based on a defect-induced multiwall carbon nanotube sensor at room temperature: Preventing Food Waste[J]. ACS Omega, 2020, 5: 30531-30537.

[30] Lucchese M M, Stavale F, Ferreira E H M, et al. Quantifying ion-induced defects and Raman relaxation length in graphene[J]. Carbon N Y, 2010, 48: 1592-1597.

[31] Ferrari A C. Raman spectroscopy of graphene and graphite: Disorder, electron–phonon coupling, doping and nonadiabatic effects[J]. Solid State Communications, 2007, 143: 47-57.

[32] Lee Y, Low M J, Yang D, et al. Ultra-thin light-weight laser-induced-graphene (LIG) diffractive optics[J]. Light: Science and Applications, 2023, 12.

[33] Hashimoto A, Suenaga K, Gloter A, et al. Direct evidence for atomic defects in graphene layers[J]. Nature, 2004, 430: 870-873.

[34] Tuinstra F, Koenig JL. Raman spectrum of graphite[J]. The Journal of Chemical Physics, 2003, 53: 1126-1130.

[35] Kumar N, Srivastava V C. Simple Synthesis of large graphene oxide sheets via electrochemical method coupled with oxidation process[J]. ACS Omega, 2018, 3: 10233-10242.

[36] Marcano D C, Kosynkin D V., Berlin J M, et al. Improved synthesis of graphene oxide[J]. ACS Nano, 2010, 4: 4806-4814.

[37] Eswaraiah V, Jyothirmayee A S S, Ramaprabhu S. Top-down method for synthesis of highly conducting graphene by exfoliation of graphite oxide using focused solar radiation[J]. Journal of Materials Chemistry, 2011, 21: 6800-6803.

[38] Vinayan B P, Nagar R, Raman V. Synthesis of graphene-multiwalled carbon nanotubes hybrid nanostructure by strengthened electrostatic interaction and its lithium-ion battery application[J]. Journal of Materials Chemistry, 2012, 22: 9949-9956.

[39] Hua W, Zhou L, Chen H. Synthesis and characterization of graphene oxide/hydrogel composites and their applications to adsorptive removal congo red from aqueous solution[J]. Journal of Physics: Conference Series.1234: 012095.

[40] Sindhu B, Kothuru A, Sahatiya P, et al. Laser-induced graphene-printed wearable flexible antenna-based strain sensor for wireless human motion monitoring[J]. IEEE Transactions on Electron Devices, 2021, 68: 3189-3194.

[41] Sharma S, Ganeshan S K, Pattnaik P K, et al. Laser-induced flexible graphene electrodes for electrochemical sensing of hydrazine[J]. Materials Letters, 2020, 262: 127150.

[42] Shaalan N M, Kumar S, Ahmed F, et al. Improvement of supercapacitor performance of in situ doped laser-induced multilayer graphene via NiO[J]. Nanomaterials, 2023, 13(14):

2081.

[43] Vivaldi F M, Dallinger A, Bonini A, et al. Three-dimensional (3D) laser-induced graphene: Structure, properties, and application to chemical sensing[J]. ACS Applied Materials and Interfaces, 2021, 13(26): 30245-30260.

[44] Sethi M, Shenoy U S, Bhat D K. A porous graphene–$NiFe_2O_4$ nanocomposite with high electrochemical performance and high cycling stability for energy storage applications[J]. Nanoscale Advances, 2020, 2: 4229-4241.

[45] Rathinam K, Singh S P, Li Y, et al. Polyimide-derived laser-induced graphene as adsorbent for cationic and anionic dyes[J]. Carbon N Y, 2017, 124: 515-524.

[46] Bhat DK, Bantawal H, Shenoy US. Rhodium doping augments photocatalytic activity of barium titanate: Effect of electronic structure engineering[J]. Nanoscale Advances, 2020, 2: 5688-5698.

[47] Ryu C, Do H M, In J Bin. Enhanced performance of densified laser-induced graphene supercapacitor electrodes in dimpled polyimide[J]. Applied Surface Science, 2024, 643: 158696.

[48] Yuan G, Wan T, BaQais A, et al. Boron and fluorine Co-doped laser-induced graphene towards high-performance micro-supercapacitors[J]. Carbon N Y, 2023, 212: 118101.

[49] Johra F T, Lee J W, Jung W G. Facile and safe graphene preparation on solution-based platform[J]. Journal of Industrial and Engineering Chemistry, 2014, 20: 2883-2887.

[50] Liu H, Xie Y, Liu J, et al. Laser-induced and KOH-activated 3D graphene: A flexible activated electrode fabricated via direct laser writing for in-plane micro-supercapacitors[J]. Chemical Engineering Journal, 2020, 393.

[51] Niu Z, Zhang L, Liu L, et al. All-solid-state flexible ultrathin micro-supercapacitors based on graphene[J]. Advanced Materials, 2013, 25: 4035-4042.

[52] Mishra N, Shinde S, Vishwakarma R, et al. MWCNTs synthesized from waste polypropylene plastics and its application in super-capacitors[J]. AIP Conference Proceedings, 2013, 1538: 228-236.

[53] Sun W, Lipka S M, Swartz C, et al. Hemp-derived activated carbons for supercapacitors[J]. Carbon, 2016, 103: 181-192.

[54] Ramachandran R, Xuan W, Zhao C, et al. Enhanced electrochemical properties of cerium metal-organic framework-based composite electrodes for high-performance supercapacitor application[J]. RSC Advances, 2018, 8: 3462-3469.

[55] Yan J, Wang Q, Wei T, et al. Template-assisted low-temperature synthesis of functionalized graphene for ultrahigh volumetric performance supercapacitors[J]. ACS Nano, 2014, 8: 4720-4729.

[56] Ardizzone S, Fregonara G, Trasatti S. “Inner” and “outer” active surface of $RuO_2$ electrodes[J]. Electrochimica Acta, 1990, 35(1): 263-267.

[57] Li Q. Effect of porosity and carbon composition on pore microstructure of magnesium/carbon nanotube composite foams[J]. Materials & Design, 2016, 89: 978-987.

[58] Alsharaeh E, Ahmed F, Aldawsari Y, et al. Novel synthesis of holey-reduced graphene oxide (HRGO) by microwave irradiation method for anode in lithium-ion batteries[J]. Scientific Reports, 2016, 6.

[59] Ye X, Yang Z, Zheng X, et al. A review on the laser-induced synthesis of graphene and its applications in sensors[J]. Journal of Materials Science, 2024, 59(26): 11644-11668.

[60] Movaghgharnezhad S, Kang P. Laser-induced graphene: synthesis advances, structural tailoring, enhanced properties, and sensing applications[J]. Journal of Materials Chemistry C, 2024, 12: 6718-6742.

[61] Cheng L, Yeung C S, Huang L, et al. Flash healing of laser-induced graphene[J]. Nature Communications, 2024, 15.

[62] Velasco A, Ryu Y K, Hamada A, et al. Laser-induced graphene micro-supercapacitors: structure, quality, and performance[J]. Nanomaterials, 2023, 13.

[63] Bhorkar K, Samartzis N, Athanasiou M, et al. Laser-assisted explosive synthesis and transfer of turbostratic graphene-related materials for energy conversion applications[J]. 2D Materials and Applications, 2022, 6: 1-13.

[64] Yang N K, Shin Y K, Park S, et al. Exploring graphene structure, material properties, and electrochemical characteristics through laser-induced temperature analysis[J]. Micro and Nano Systems Letters, 2024, 12.

[65] Santhosh R, Raman S R S, Krishna S M, et al. Heteroatom doped graphene based hybrid electrode materials for supercapacitor applications[J]. Electrochimica Acta, 2018, 276: 284-292.

[66] Zhang L, Zhang F, Yang X, et al. Porous 3D graphene-based bulk materials with exceptional high surface area and excellent conductivity for supercapacitors[J]. Scientific Reports, 2013, 3(1): 1-9.

[67] Asghar M, Zahra S A, Khan Z, et al. Laser-Assisted fabrication of nanostructured substrate supported electrodes for highly active supercapacitors[J]. Frontiers in Materials, 2020, **7**.

[68] In J Bin, Hsia B, Yoo JH, et al. Facile fabrication of flexible all solid-state micro-supercapacitor by direct laser writing of porous carbon in polyimide[J]. Carbon, 2015, 83: 144-151.

[69] Tariq H, Awan S U, Hussain D, et al. Enhancing supercapacitor performance through design optimization of laser-induced graphene and MWCNT coatings for flexible and portable energy storage[J]. Scientific Reports, 2023, 13: 1-13.